Proceedings of the ASME 2010 3rd Joint US-European Fluids Engineering Summer Meeting and 8th International Conference on Nanochannels, Microchannels, and Minichannels
FEDSM-ICNMM2010
August 1-5, 2010, Montreal, Canada

FEDSM-ICNMM2010-30757

EXPERIMENTAL AND COMPUTATIONAL FLOW AND TEMPERATURE FIELDS IN A HEAT EXCHANGER CRYSTALLIZER GEOMETRY FOR VALIDATION AND IMPLEMENTATION OF A NOVEL PROCESS SENSOR

Marcos R. Pascual
Process and Energy Laboratory, Delft University of Technology
Delft, Zuid Holland, The Netherlands

Herman J. M. Kramer
Process and Energy Laboratory, Delft University of Technology
Delft, Zuid Holland, The Netherlands

ABSTRACT

During crystallization processes the control and effective distribution of heat transfer from the heat exchanger to the solution plays an important role. The turbulent flow field and the temperature variations in the solution determine the local supersaturation profiles and the spatial particle distribution. Thus they have a strong impact on the final product quality, production capacity and efficiency of the process.

In this sense, a sensor able to determine in situ the local process variables to get better insight in the process behavior, would be required. The recently proposed Smart moving Process Environment Actuators and Sensors (Smart PEAS) is a promising initiative to achieve a more efficient process control. In this PEAS system a network of floating sensors is integrated using Ultra Wide Band (UWB) wireless technology to form a monitoring and control system

As a first phase in the development of the Smart PEAS, the research is focused on the accurate measurements of the flow field and local temperature distribution in a reactor.

The hydrodynamics of the Smart PEAS are very important to achieve the necessary accurate process information. In order to determine the hydrodynamic characteristics of the Smart PEAS and to validate and compare the obtained results, laternative non intrusive techniques are used to investigate them in this work.

Microencapsulated liquid crystals are used as a measurement technique to study the local temperature and flow field in a heat exchanger crystallizer geometry. To measure the 3D flow and temperature fields the microencapsulated liquid crystals are recorded in a sheet of light plane inside the crystallizer by two digital color cameras in a stereoscopic position. The images of the liquid crystals are correlated to obtain the three velocity components (3C), while from the colors of the microencapsulated liquid crystals the local temperature can be deduced after appropriate calibration.

Parallel experiments are done to investigate the three dimensional trajectories of different sensor geometries in the equipment by direct visualization of the sensors.

Computational fluid dynamics simulations are performed to calculate the flow field, temperature distribution and sensor trajectories. The results are compared with the experimental results for validation.

The validation of the computational simulation results with the experiments gave the necessary confidence to predict flow fields in new crystallizer designs.

On the basis of the analysis the Smart PEAS sensor design and the reliability of the measurements obtained can be compared and implemented.

INTRODUCTION

In a large number of crystallization processes from solution or from the melt, the supersaturation is achieved by the action of heat exchangers. In industrial continuous crystallization processes, where liquid is constantly fed into the crystallizer, this results in supersaturation profiles close to the heat exchanger (HEX) wall and around the feed points. Especially in large scale equipment these profiles in the process conditions severely affect the product quality and process performance and are difficult to avoid or to control due to the lack of process knowledge and adequate measurement techniques. Current measurement and control methods are based on measurements at a single or a few fixed positions and therefore provide insufficient information.

The use of smart moving process environment actuators and sensors (PEAS) inside the process equipment can provide a solution to obtain accurate three-dimensional profiling of these process parameters. To realize this, the smart floating sensors will be equipped with ultra wideband (UWB) wireless transceivers for communication and localization.

With this local information obtained from the process equipment, unwanted temperature or flow distributions can be easily detected and controlled. Moreover this information can give additional information to improve the design of the equipment.

In order to validate the floating sensor concept and to estimate the accuracy of the measurements by the PEAS alternative, non intrusive methods will be used. In this paper we will focus on the modeling and experimental validation of the two main responsible factors to control the local supersaturation in cooling crystallizers, circulation flow and temperature.

As an example crystallizer for these studies a scraped heat exchanger crystallizer with a scraped flat bottomed cooling surface was used. This crystallizer was specially designed to investigate ice scale formation from an aqueous electrolyte solution by Vaessen et al. [1] and Pronk et al. [2] during cooling and eutectic freeze crystallization.

As a non intrusive technique to measure the flow field in the crystallizer Particle Image Velocimetry (PIV) is perfectly suitable and even more so when the used tracer particles are microencapsulated liquid crystals that at the same time give information of the local velocities and temperatures.

Several reviews on the topic of liquid crystal thermometry has been produced [3-12], and an extensive information on digital particle image thermometry velocimetry methodology (DPIT/V) can be found in the review by Dana Dabiri[13] that includes a background on liquid crystals and color theory, a discussion of experimental setup parameters, a description of the methodology's most recent advances and processing methods affecting temperature measurements, and an explanation of its various implementations and applications.

Applications of liquid crystal thermometry have been investigated in stirred vessels by LEE and YIANNESKIS[14] and Wang[15-17].

On the study of our crystallizer temperature and flow fields 3C-DPIV/T will be used. DPIT/V is relatively new, its applications and implementations are few. In developing the scanning DPIT/V method, Fujisawa and Funatani[18] have mapped a three-dimensional turbulent thermal convection flow field. Towards this end, they were able to map the resulting plume structures within the flow field. In combining this technique with stereo DPIV, Fujisawa et al.[19,20] have further mapped the development of plume structures within a three-dimensional turbulent thermal convection flow field. Fujisawa et al.[21] have also investigated the spokes structures of unsteady non penetrative turbulent thermal convection within a horizontal fluid layer.

One of the characteristics of the Smart PEAS sensors is their UWB communication with each other and with fixed beacons which allows the localization of the sensors. To validate this localization of the sensors inside the reactor, 3D particle image tracking is used.

Multiphase visualization to investigate the degree of disturbance inside the flow field is also performed.

These experimental validations of the Smart PEAS sensor are compared with a home written computational fluid dynamics code based in Lattice Boltzmann scheme. In this case the validation of the CFD code will allow us in further stage of the Smart PEAS sensor to (based in its experimental results) implement and develop new crystallizers or industrial process equipment.

SMART PEAS HYDRODYNAMIC GEOMETRY

The accuracy of the monitoring of the process parameters with the floating Smart PEAS will not only depend on the accuracy of the local measurement by the sensor but also on the accuracy of the positioning as well as on the flow characteristics in the process equipment. The hydrodynamic design characteristics of the sensors will determine for example how often and under what conditions the sensor will visit a particular part of the process equipment, being able to choose a particular area based on how relevant this information is for the process.

Thus to design the sensor hydrodynamic geometry, the flow characteristics should more or less be known a priori. Based on the physical flow field characteristics the geometry and the density distribution of the Smart PEAS sensor can be tuned to investigate specific areas inside the equipment. As an example of common requirement it will be that the sensor actually travels around all the equipment with a minimal disturbance, following the flow inside the equipment and not colliding with hardware such as impellers or walls. For this configuration the most appropriated geometry is a sphere with uniform density distribution due to its total symmetry. To impose that the particles follow the flow and do not collide with the hardware the Stokes number for the particles at the particular configuration must be lower than 1. Other cases where specific areas will be investigated will require different geometries and density distributions.

Another aspect of the smart PEAS sensors that needs validation is the position of the sensors as function of the time.. The real sensor UWB based localization algorithm will consist in a two-step procedure. To localize a sensor in a sensor network, first the mutual distances between sensors will be computed. Secondly the sensor positions are estimated according to the range information obtained in the first step[22].

To validate and obtain the relative accuracy of the system 3D image particle tracking is used. The experimental setup consisted of a cylindrical baffled vessel stirred with a rushton turbine, and provided with a heat exchanger on the bottom. The vessel is placed inside a glass cube filled with liquid to minimize optical disturbances. The sketch with distances in cm is shown in Fig.1.

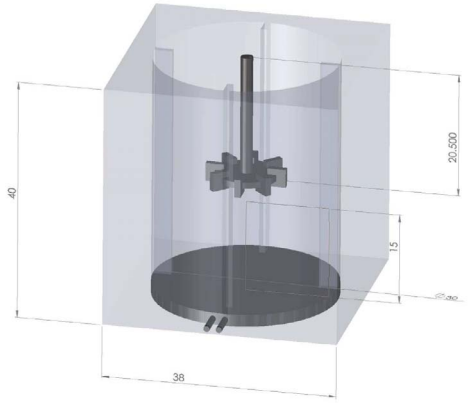

Figure 1. cylindrical, baffled vessel stirred with a rushton turbine in a glass cube filled with liquid to minimize optical disturbances.

To obtain the 3D data and track the particle sensors, the inside of the tank was recorded with a high speed camera. The camera was focused perpendicular to one face of the glass cube to record the plane z-x, and with the help of one mirror positioned with an angle of 45 ^{o} with respect the consecutive perpendicular face the plane z-y was recorded (Fig.2)

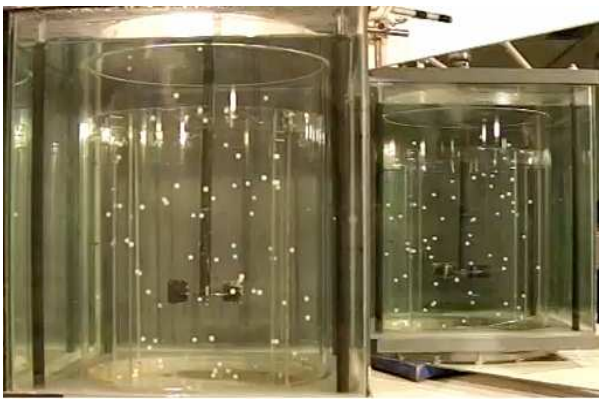

Figure 2. Front face (left) and mirrored perpendicular face (right) to obtain the 3D in formation by particle image tracking processing.

The experiment was done with several dummy sensors as that can be also the real case, and the capability of differentiate them should be tested.

The images were processed using a script in Matlab. The code reads the original image and eliminates the color range that does not correspond with the particle color. Then the left areas are read and the not wanted parts based in a maximum and minimum possible area, the eccentricity and the coefficient between height and width are eliminated. Once the particles are detected in the image, the positions of the individual particles are matched with their mirror positions to obtain the 3D position.

The individual particles are flagged and followed with the 3D position information, obtaining the 3D trajectories on time and being able to calculate their velocities and their accelerations. An example of three different particles followed on time is presented in Fig.3.

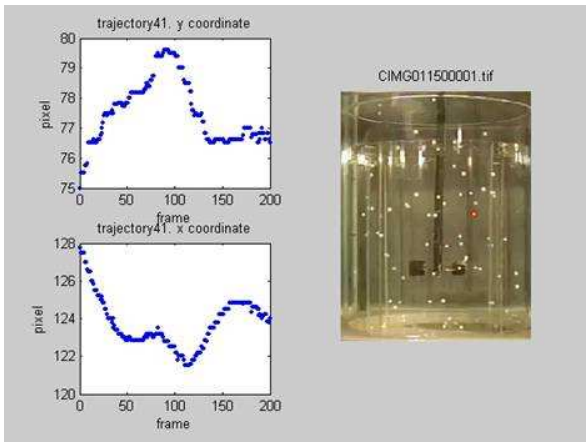

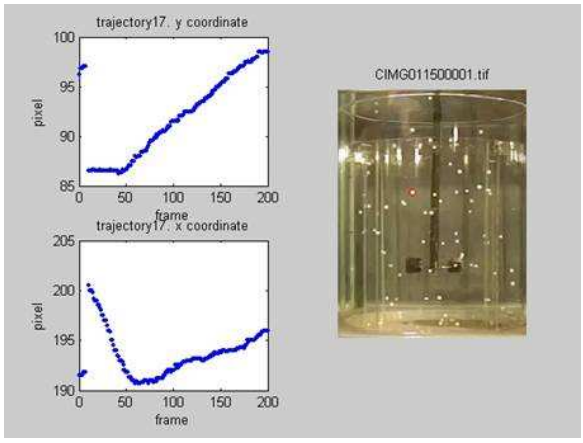

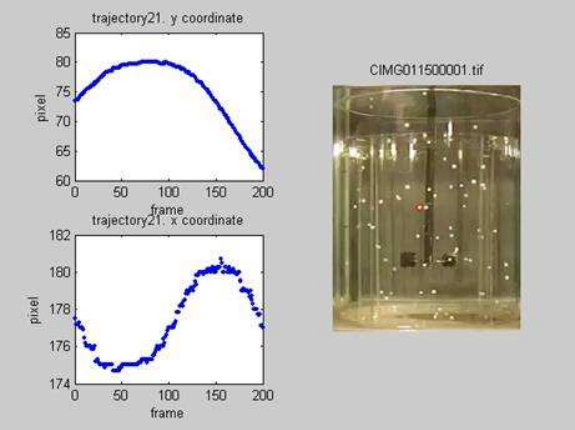

Figure 3. Graphs show the x and y position trajectories of a particular sensor in the pixel frame picture (position) versus frame (time). The followed particle is circled in red at the raw image beside the trajectories.

Another important aspect of the geometrical design the disturbance of the flow by the presence of the sensor. For this analysis a multiphase studied is needed. Using the advantage of white light illumination the and high speed color cameras, the flow can be measured by small particles colored differently than the sensor particle to be differentiated during processing of the images for particle image velocimetry, where the sensor particles can be filtered, and for particle tracking where the tracer flow particles are filtered instead. An example of disturbance on the flow by the particle sensor is shown in Fig. 4.

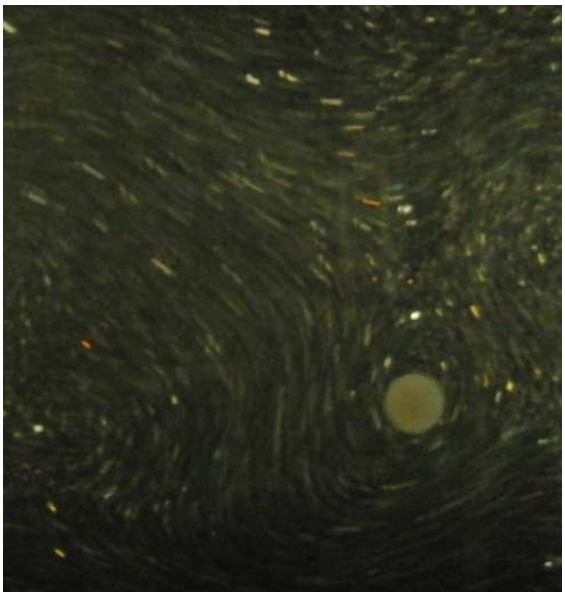

Figure 4. The flow disturbance patent can be appreciated by the visualization of the flow tracer particles around the particle sensor of 5 mm diameter.

EXPERIMENTAL 3C DPIV/T CRYSTALLIZER SETUP

For the validation studies we used an experimental set-up, designed for the study of ice-scaling during freezing and eutectic freeze crystallization of aqueous solutions. The crystallizer consists of a 10 liter vessel of 200 mm diameter and 300 mm height with a scraped HEX surface at the bottom as shown in Figure 1. The 1 mm thick stainless steel bottom plate has a heat transfer area of 0.031 m^2, which is scraped by four rotating Teflon scraper blades of 99 mm driven by a vertical shaft. Halfway this shaft, a turbine mixer with a diameter of 100 mm is installed to keep the slurry well mixed. The HEX plate is cooled underneath by a 50 wt% potassium formate solution. The coolant flows at a high flow velocity through a coupled inlet/outlet spiral channel below the HEX plate to avoid temperature differences across the HEX surface. The height and width of the channel are 5 and 17 mm respectively. The flow velocity of the coolant in the channel is over 3 m/s, which guarantees turbulent channel flow. The HEX inlet temperature is controlled within 0.1 K by a cooling machine.

To study a continuous process, a feed flow enters the vessel at a height of 200 mm from the bottom. The crystallizer then overflows to an ice-melting vessel where the solution is heated, and from which the aqueous solution is pumped back to the crystallizer through the feed flow, thus creating stationary flow conditions. To minimize heat leakage to the surroundings, the experimental set-up was thermally insulated wherever appropriate.

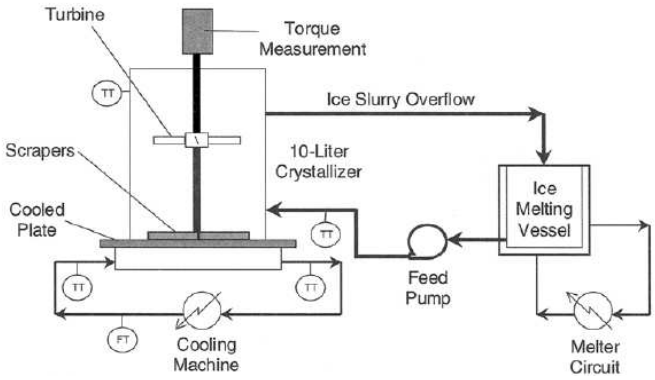

Figure 5. Flow scheme of the continuous cooling experiments[1].

The temperatures of the coolant at the inlet and outlet, the temperature of the solution close to the top and the bottom of the crystallizer at the height of 45 and 220 mm, 15 mm inside the crystallizer from the wall, as well as the temperature of the feed flow were measured with an ASL F250 precision thermometer connected to PT-100 temperature sensors with an accuracy of ±0.01 °C. The pressure of the coolant in the channel was measured at the inlet and outlet by two Rosemount

pressure transmitters with an accuracy of ±0.001 bar. The flow rate of the feed solution and the coolant were measured by two Rosemount E-series magnetic flow meters with an accuracy of ±1 l/h. The five temperatures, the two pressures and the two flow rates were recorded every 1 second by a computer using a data acquisition program.

Flow fields in stirred vessels have been extensively reported in the literature. The consequent temperature profiles of some particular devices have been reported [14-17]. To perform the stereoscopic DPIV/T measurements some extra considerations have to be taken into account. The principal difference is the necessity of white light illumination. This is because the color of the liquid crystal tracers needs to be recorded in order to be analyzed and to obtain the temperature profiles.

High intensity white light source is needed as only the scattered light from the tracer particles will be recorded by the cameras. It is reported in literature[13] that halogen or Xenon lamps of around 1KW and Xenon strobe flash lamps of 2-8J output are used for this purpose.

The light sheet(s) created by continuous lamps can also be mechanically strobed as reported by Fusikawa[19], although the pulses can not be so short as with strobes. This limits the experimental conditions or the accuracy and resolution.

The choice of the particle diameters for the encapsulated liquid crystal depends on the velocity and turbulent flow to measure. In the case of turbine blades, similar to our stirred tank, the recommended size varies between 50–240 μm[13].

This creates some additional problems. First the angle between illumination and visualization influences the recorded color by the camera. The geometry surface influences the angle of reflection from the incident light, increasing even more this behavior. This can be partially overcome by choosing the sheet light width on basis of the tracer's sizes.

In the case of recording the temperature of the dummy sensor surface by coating the particle with sprayable liquid crystal the effect is even higher and complicates the calibration between hue and temperature values due to the angle of incident illumination and the recorded observation angle, on the spherical surface. This can be solve by calibration at a stable temperature of the observed colors in the sensor surface at the different positions of the observed area. Knowing then the gradient of variation on the surface color by the angle of observation from the camera and the tangential angle of the point at the surface the real temperature can be calculated.

Also if the intensity of white light scattered from the rounded surface is too high already color tones are created as can be observed in Fig.6 with white particles.

Therefore accurate calibration taking into account these effects is essential to be able to avoid errors. Calibration experiments were these issues are determined allow us to reconstruct the real values by subtracting or correcting the distorted values during the post processing of the images.

Figure 6. a) Colored scattered light from particles of around 25 μm diameter. b) Colored scattered light from a sphere of 5 mm diameter.
Remarks: In both cases the light sheet is coming from the left side. Case b) has a higher illumination intensity than a)

Another point is that the amount of heat transmitted into the illuminated area to obtain sufficient scattered light intensity is really high and can affect our measurements. In this case to avoid thermal influences the illumination time during the measurements can not exceed more than 5 sec.

CFD FLOW AND PARTICLE TRAJECTORIES VALIDATION

To validate our CFD flow results, the flow field and the turbulence distribution inside the crystallizer were investigated by a laser Stereoscopic Particle Image Velocimetry, (3C-PIV). A general description of 3C-PIV can be found in Raffel et al.[23] and specific details of the 3C-PIV set-up used here can be found in Ravelet et al. [24]. This set-up is sketched in Fig.7.

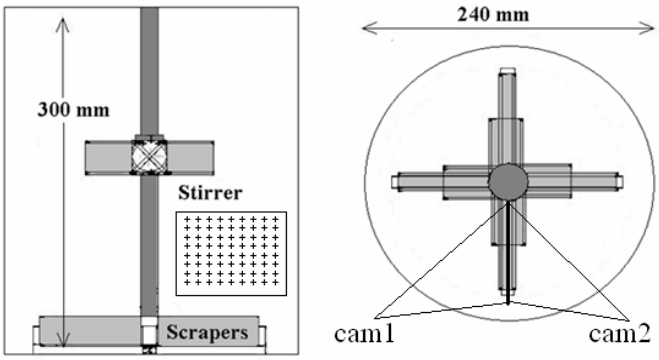

Figure 7. Sketch of set-up for PIV measurements with a PIV calibration grid-image inside.

The shaft with scraper and stirrer was taken from the original crystallizer geometry with a 200 mm internal diameter and put into a slightly larger glass cylinder with a 240 mm internal diameter, which was well aligned in the two-camera stereoscopic PIV set-up described by Ravelet et al. [24] .With the vertical-radial laser light sheet two 2D PIV images were captured from two different cameras at different positions, which represent two different projections of the particle motion. The 3D calibration, the laser and camera timing as well as the PIV image processing were all done using a commercial hardware and software. The measured 2D area inside the cylinder was 45 mm high and 80 mm wide, and started just above the scraper and at the outer wall, as shown in the left hand picture of Figure 7.

The Navier-Stokes equations governing the flow in the stirred tank were discretized according to the lattice-Boltzmann method. This is an inherently parallel and efficient numerical scheme for computational transport physics[25]. The strong turbulence generated by the impeller and scrapers prohibits direct numerical simulation: the computational effort for resolving all length and time-scales would be too large.

In large-eddy simulations only the large-scales are resolved explicitly – the rationale behind it is that the small scales behave more universally and are therefore more prone to modeling than the large scales[26]. Modeling instead of resolving the small scales alleviates the computational burden. For modeling of the small scales the standard Smagorinsky subgrid scale model was applied. A value of c_S=0.12 was adopted as the Smagorinsky constant, which is within the range of values commonly used in shear-driven turbulence.

The stirred-scraped crystallizer computational domain configuration consists of a cylindrical, flat-bottomed, tank with diameter of 240 mm and a height of 300 mm as in the 3C-PIV experiments.

The uniform, cubic grid inherent to most of the lattice-Boltzmann formulations comprised $1.8\cdot10^7$ nodes. In terms of spatial resolution: the linear size of a cubic lattice cell amounted to approximately 1 mm. The time step in the LES was such that one impeller revolution took 4200 time steps.

The Reynolds number that fully determines this single-phase flow is defined as $Re=ND^2/\nu$ with *N* the impeller speed in rps, D the diameter of the scraper and ν the kinematic viscosity of the working fluid. The continuous phase was water with a density = 10^3 kg/m^3 and, at the constant temperature of the 3C-PIV experiment of 20 ^{o} C, $\nu = 10^{-6}$ m^2/s. The scraper and impeller were set to rotate at a speed of 77 rpm corresponding to $Re=5\cdot10^4$.

The LES is started from a zero velocity field. In the start-up phase of the flow we monitor the total kinetic energy in the tank. Once this has stabilized we start collecting flow data for later statistical analysis such as average velocity and turbulent kinetic energy fields.

The flow field as measured by 3C-PIV for the middle section of the crystallizer showed that in the core around the shaft the absence of a radial and axial mean flow. From about 60 mm from the shaft, there is a secondary flow in the radial axial plane. From 60 to 100 mm the fluid flows downward, and from 105 mm to the wall the fluid flows upwards (Fig.8).

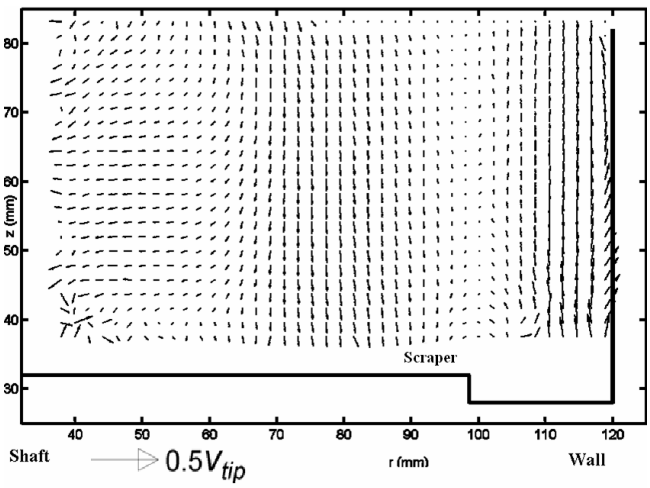

Figure 8. Time averaged radial and axial velocities measured by 3C-PIV depicted as vectors with their length proportional to their norm

In Figure 9 the dash-dotted line represents the tangential velocity of the scraper. The solid line representing the time-axial averaged flow measured by the PIV, suggests that the solution is in solid body rotation up to about 40 mm from the shaft. When moving radially outward, the flow tends to conserve its angular momentum; hence the tangential velocity quickly decreases (in a frictionless flow this would lead to a 'potential vortex' [27].As a simplified physical model of the flow, we fitted the measured tangential velocity profile with the Oseen vortex solution[27], which gradually transits from a solid-body rotation in the inner region to a free vortex flow in the outer the region. The transition takes place at approximately r=40mm, as shown in Figure 9. The measured tangential flow matches qualitatively with the vortex flow in the Oseen model.

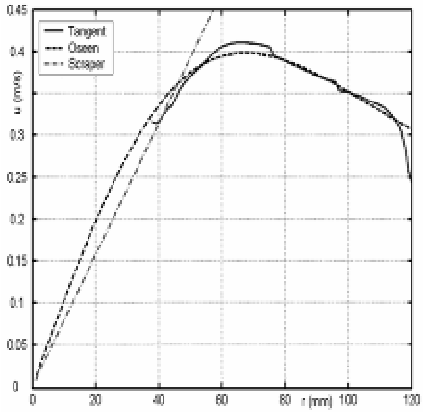

Figure 9. Measured time-axial averaged tangential velocity of the PIV area, the scraper velocity and the tangential velocity calculated from the best fit Oseen vortex

Fig.10a shows the axial and radial time averaged velocities for the whole tank as obtained from the LES computational simulations, after steady-state was achieved and therefore the total kinetic energy was constant, plotted as vectors with length normalized. To validate the computational results we compare the simulated flow velocities with the velocities obtained from the 3C-PIV measurements in the same middle region of the crystallizer. This region is indicated in Fig.10a by a black rectangle at the right hand side of the picture.

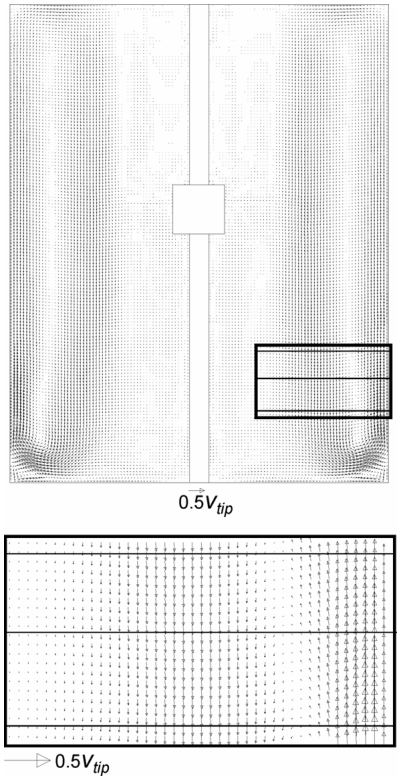

Figure 10. a) Time averaged velocity vectors of the flow field inside the scraped heat exchanger crystallizer. The black rectangle corresponds to the area measured by 3C- PIV. b) Computational results of the 3C- PIV measured area. The three lines across the measured area are drawn at heights of 45, 59 and 75 mm from the bottom plate.

Zooming in on the simulations of the flow velocities in the PIV measured area in Fig.10b demonstrates that also in the simulations axial or radial flow is nearly nonexistent near the shaft. The middle area shows a strong axial flow towards the bottom with a negligible radial contribution. Close to the outside wall the flow is carried upwards with also little radial contribution, so these results are in good agreement with the stereoscopic PIV data. The flow velocities at the three lines across the measured area at three different heights of 45, 59 and 75 mm from the bottom plate are presented in Fig.11.

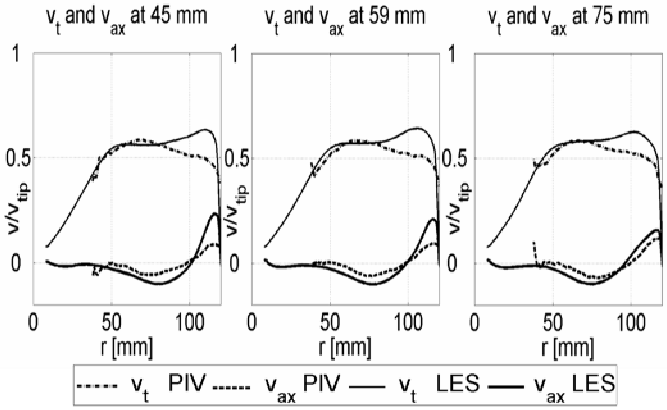

Figure 11. Tangential and axial velocities calculated from 3C-PIV experiments and from LES simulations at heights of 45, 59 and 75 mm from the bottom plate. Velocities are normalized with scraper tip speed.

The tangential and axial velocities at the three heights are plotted against those calculated from the stereoscopic PIV experiments. The results match quite well, although the tangential and axial velocities from the PIV experiments are slightly smaller than the LES values. Also the tangential velocities decrease when approaching the outside wall, while the LES values increase slightly before decreasing at the wall. The agreement is however in general very satisfactory, and the observed differences can be explained by the unavoidable inaccuracies in the experimental results and by the idealized computational approach.

A qualitative comparison between the PIV and LES snapshots of the same portion of the flow (Fig.12 and Fig.13) show interesting resemblance. Clearly turbulence is much stronger close to the outer tank wall. Furthermore the sizes of the turbulent structures observed in PIV and LES agree quite well.

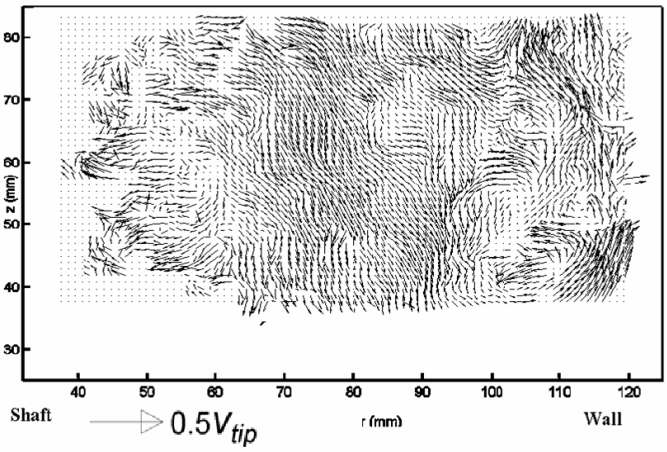

Figure 12. Instantaneous capture of the flow from the 3C-PIV measurements. Vectors represent the axial and radial velocity and their length proportional to their norm.

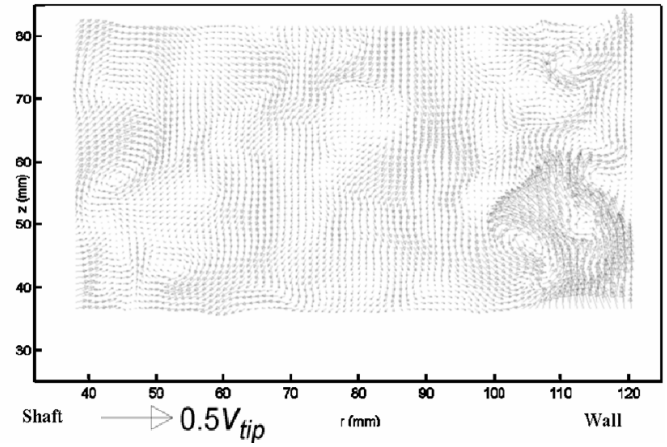

Figure 13. Instantaneous capture of the flow from the LES simulations. Vectors represent the axial and radial velocity and their length proportional to their norm.

To validate the particle behavior a simplified model in the scraper area is used and the Navier-Stokes equations are solved without the use of a turbulence model. Every grid cell corresponds to 1 mm in each direction.

As boundary conditions the domain walls are made periodic in their x and y directions and for the bottom plane (scraped surface) a no-slip condition is applied. The scraper extends from one side of the box to the other in the x direction and moves in the y direction. Since a periodic boundary condition was applied in the y direction, we mimic the scraper meeting its own back flow as if this flow were produced by the scraper in front as happens during rotation. For the top plane of the computational domain a free slip condition is applied. The particles that arrive there are not taken into account anymore just as if they left the scraping area to the bulk and do not come back. The Reynolds number is defined as Re=V L/υ , with V the scraper speed L the scraper height and υ the kinematic viscosity of the working fluid. In the cases we studied the Reynolds number was set to Re = $2.5 \cdot 10^4$, which makes the flow turbulent. The continuous phase was water with a density = 10^3 kg/m^3 and viscosity = 10^{-6} m^2/s. For the simulations the two scraper geometries as described in the experimental section were used.

As already mentioned, the simulations were performed in a linearly moving system instead of in a rotating system as were the experimental visualizations. Thus we leave out the effects of coriolis forces in the fluid flow and the centrifugal and coriolis forces on the particles (given their density difference with the liquid). These effects could have been incorporated in the simulations by adding a body force to the fluid flow equations, and additional forces acting on the particles. In this qualitative stage of research it was decided to focus on flow structures and leave refinements for future work. In terms of the particle flow around the scraper, we do not expect much effect of the centrifugal force since it would act in the x-direction, whereas we observe the flow past the scraper in the yz-plane.

The particle trajectories were calculated in a Lagrangian framework. A simple approach was undertaken in which we restricted the forces acting on the spherical particles with diameter d_p to inertia, gravity and drag forces. The equation of motion used was:

$$\frac{\pi}{6} d_p^3 \rho_p \frac{d\vec{v}_p}{dt} = \frac{\pi}{8} d_p^2 \rho_l C_D \left|\vec{u} - \vec{v}_p\right| \left(\vec{u} - \vec{v}_p\right) + \frac{\pi}{6} d_p^3 \left(\rho_p - \rho_l\right) \vec{g} \qquad (1)$$

$$\frac{d\vec{x}_p}{dt} = \vec{v}_p \qquad (2)$$

The velocity **u** vector of the fluid at the particle position is calculated by tri-linear interpolation of the surrounding grid velocities. For the drag coefficient we took the Schiller and Naumann[28] correlation:

$$C_D = \frac{24}{\mathrm{Re}_p} \left(1.0 + 0.15\,\mathrm{Re}_p^{0.687}\right) \quad \mathrm{Re_p}<1000 \qquad (3)$$

and

$$C_D = 0.44 \qquad \mathrm{Re_p} \geq 1000 \qquad (4)$$

where

$$\mathrm{Re}_p = \left|\vec{u} - \vec{v}_p\right| \frac{d_p}{\nu} \qquad (5)$$

The system of equations was numerically solved using semi implicit Euler time stepping. For easy visualization only 200 particles were released at the bottom of the flow domain in front of the scraper. They were treated as spherical particles of d_p= 1 mm diameter and had the properties of $MgSO_4 \cdot 7H_2O$ crystals as in the experimental part. The Stokes number (defined as $St = \frac{\rho_p}{\rho_l} \frac{d_p^2 V}{\nu L}$) for these particles is around 3 (larger than 1) what implies they have sufficient inertia to collide with the scraper and bottom wall. The collisions with the scraper and the bottom were taken to be elastic. This means that for particle

collision with the bottom the velocity component in the z direction of the particle changes from v_p to $-v_p$, leaving the x and y components as before the collision. The final direction of particle collisions with the scraper depends on the inclination angle of the wall and the incident angle of the particle. The outgoing particle angles after colliding with the scraper only vary in the y-z plane, the velocity in x direction does not change after the collision. Since the scraper is moving in the y-direction, collisions with the scraper add momentum to the particles in the y direction.

The method for detecting and handling particle-particle collisions was similar to the one proposed by Chen et al.[29]. In their method, they make use of a collision detection algorithm that anticipates collisions in the upcoming time step. Subsequently, the path of two particles that are bound to collide is integrated in a three-step-process: the pre-collision step, the collision step (in which the particles exchange momentum), and the post-collision step. In order to limit the computational effort spent in handling the particle-particle collisions (which in principle is an M^2 process, with M the number of particles) we have grouped the particles in each other's vicinity in a so-called link-list[30]. The extent of the vicinity of a particle in which potential collision partners are sought is the lattice cell in which the particle under consideration resides, and the 26 neighboring cells. This reduces the number of possible collisions partners to a few for a specific particle during a specific time-step.

The collision algorithm assumes that one particle can only collide once during one time step. The reason is purely practical: taking into account multiple collisions in one time step would lengthen the computations to an unfeasible extent. The assumption either limits the time step, or the particle volume fraction. In any case, in the simulations there is a finite chance that the collision detection algorithm misses a collision. This is reflected in the situation that at the next time step, two approaching particles have a mutual distance less than d_p. If this occurs, a so-called missed collision procedure is executed: directly at the start of the time-step, the particles involved are given their post-collision velocities (making that they now are moving apart). During the time step, the particles are displaced as a pair according to their average velocity, and they move apart with their relative velocity until they have a mutual separation of at least d_p. Visual comparison between the computational and experimental results are shown in Fig.14.

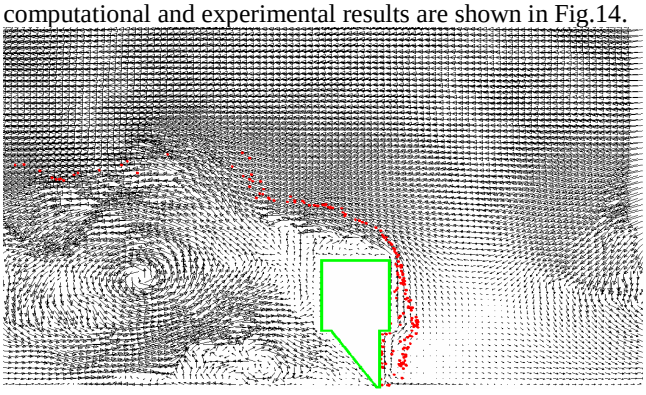

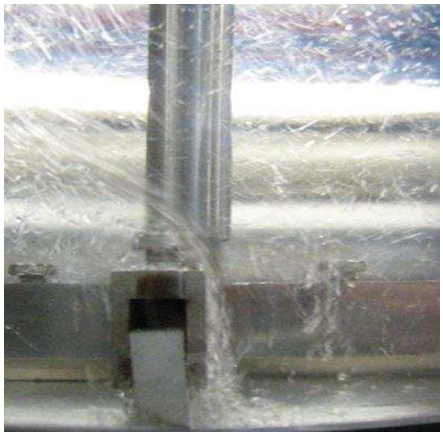

Figure 14. a) Computational results (left) with scraper sketch colored in green and the particles in red. b) Experimental visualization.

CONCLUSIONS

Different techniques have been presented as non intrusive methods to validate the data information sent by the Smart PEAS sensor during operating process equipment.

As example geometries for the experimental validation a continuous crystallizer design for EFC crystallization and a batch crystallizer with better optical access were chosen.

The capability to validate the positioning of the Smart PEAS sensors was studied by particle image tracking of a bench of dummy spherical sensors in the batch crystallizer. The multiphase studies to measure the disturbance of the flow by the Smart PEAS sensor was proposed and preliminary visualizations presented.

The 3C-PIV/T setup characteristics for the validation of the temperature readings of the sensor were presented. The system gives an alternative non intrusive method to characterize the flow and temperature fields of the process in situ, for the validation of the Smart PEAS data, or a priori, for the design of the sensor. In order to be able to further develop and implement the process equipment based in the measured information of the Smart PEAS sensor a home CFD code based in Lattice Boltzmann scheme is being developed. Comparison results of the measured by 3C-PIV flow field and particle trajectories visualizations are presented for a continuous crystallizer.

ACKNOWLEDGMENTS

This research is supported by the Dutch Technology Foundation (STW) applied science division of NOW and the Technology Program of the Ministry of Economical Affairs.

We acknowledge the input of Prof Dr. Jos Derksen for his support in the development of the CFD simulations.

REFERENCES

1. Vaessen, R.J.C., Himawan, C. and Witkamp, G.J., 2002, "Scale formation of ice from electrolyte solutions on a scraped surface heat exchanger plate." Journal of Crystal Growth, **237-239 (1-4 III)**, pp. 2172-77
2. Pronk, P., Infante-Ferreira, C.A., Rodriguez Pascual, M. and Witkamp, G.J., 2005, "Maximum temperature difference without ice-scaling in scraped surface crystallizers during eutectic freeze crystallization." Proc. 16th Int. Symp. on Industrial Crystallization. pp. 1141-46.
3. Moffat, R.J., 1990,"Some Experimental Methods for Heat Transfer Studies", Exp Therm Fluid Sci **3**, pp.14–32.
4. Baughn, J.W., 1995, "Liquid crystal methods for studying turbulent heat transfer.", Int. J. Heat Fluid Flow **16**, pp. 365–375
5. Roberts, G.T., East, R.A., 1996, "Liquid crystal thermography for heat transfer measurement in hypersonic flows: a review." J Spacecr Rockets **33**, pp.761–768
6. Wozniak, G., Wozniak, K., Siekmann, J., 1996, "Non-isothermal flow diagnostics using microencapsulated cholesteric particles." Appl Sci Res **56**, pp.145–156
7. Behle, M., Schulz, K., Leiner, W., Fiebig, M., 1996, "Color-based image processing to measure local temperature distribution by wideband liquid crystal thermography." Appl. Sci. Res. **56**, pp.113–143
8. Stasiek, J., 1997, "Thermochromic liquid crystals and true colour image processing in heat transfer and fluid-flow research." Heat Mass Transf. **33**, pp. 27–39.
9. Stasiek, J., Stasiek, A., Jewartowski, M., Collins, M.W., 2006, "Liquid crystal thermometry and true-colour digital image processing." Opt Laser Technol **38**, pp. 243–256
10. Stasiek, J.A., Kowalewski, T.A., 2002, " Thermochromic liquid crystals applied for heat transfer research." Opto-electron Rev. **10**, pp. 1–10.
11. Smith, C.R., Sabatino, D.R., Praisner, T.J., 2001, "Temperature sensing with thermochromic liquid crystals." Exp. Fluids **30**, pp.190–201.
12. Kowalewski, T.A., Ligrani, P., Dreizler, A., Schulz, C., Fey, U., Egami, Y., 2007, "Temperature and heat flux." In: Tropea, C., Yarin, A.L., Foss, J.F. (eds) Springer handbook of experimental fluid mechanics, 1st edn. Springer, Berlin, pp. 487–561.
13. Dabiri, D., Exp. Fluids, 2009, "Digital particle image thermometry/velocimetry: a review." **46**, 191–241.
14. Lee, K.C., Yianneskis, M., 1997, "A liquid crystal thermographic technique for the measurement of mixing characteristics in stirred vessels", Trans IChemE, **75**, Part A.
15. Wang, Z.-F., Huang, X.-B., Shi, L.-T., 2002, "Study on the unsteady temperature profiles in an agitated tank equipped with different types of impeller." Gao Xiao Hua Xue Gong Cheng Xue Bao/Journal of Chemical Engineering of Chinese Universities **16** (6), pp. 609-613 .
16. Wang, Z., Huang, X., Shi, L., Ma, Q., 2002, "Measurement and numerical simulation of temperature distributions in agitated tank equipped with PBT impeller", Huagong Xuebao/Journal of Chemical Industry and Engineering (China), **53** (11), pp. 1175-1181.
17. Wang, Z.-F., Huang, X.-B., Zhou, G.-Z., Shi, L.-T., 2001, "Temperature distributions in an agitated tank heated by vertical pipes ",Huabei Gongxueyuan Xuebao/Journal of North China Institute of Technology, **22** (6), pp. 416-419.
18. Fujisawa, N., Funatani, S., 2000, "Simultaneous measurement of temperature and velocity in a turbulent thermal convection by the extended range scanning liquid crystal visualization technique.", Exp. Fluids **29**, pp.158–165.
19. Fujisawa, N., Funatani, S., Katoh, N., 2005, "Scanning liquid-crystal thermometry and stereo velocimetry for simultaneous three dimensional measurement of temperature and velocity field in a turbulent Rayleigh–Benard convection." Exp. Fluids **38**(3), pp. 291–303.
20. Fujisawa, N., Watanabe, M., Hashizume, Y., 2008, "Visualization of turbulence structure in unsteady non-penetrative thermal convection using liquid crystal thermometry and stereo velocimetry." J Vis **11**, pp. 173–180
21. Fujisawa, N., Funatani, S. and Watanabe, Y., 2008, "Simultaneous Imaging Techniques for Temperature and Velocity Fields in Thermal Fluid Flows.", Journal of Visualization,**11**(3) ,pp.247-255.
22. Irahhauten, Z., Leus, G., Nikookar, H. and Janssen, G.. UWB Ranging Based on Partial Received Sub-Band Signals in Dense Multipath Environments. To appear in Proc. of the International Conference on Communications (ICC 2010), Cape Town, South-Africa, May 2010.)
23. Raffel, M., Willert, C. and Kompenhans, J., 1998, " Particle Image Velocimetry", Springer
24. Ravelet, F., Delfos, R. and Westerweel, J., 2007, "Experimental studies of liquid liquid dispersion in a turbulent shear flow." paper 145 for TSFP-5, Munich, August 27-29
25. Succi, S., 2001. "The lattice Boltzmann equation for fluid dynamics and beyond.", Clarondon Press, Oxford.

26. Lesieur, M., Métais, O., 1996. “New trends in large-eddy simulations of turbulence.” Annu. Rev. Fluid Mech., **28**, pp. 45-82.
27. Batchelor, G.K. , 1967, “An Introduction to Fluid Dynamics.” Cambridge University Press
28. Schiller, L., Naumann, Z.,1935, “A drag coefficient correlation.”, Z. Ver. Deutsch. Ing. pp.77-318
29. Chen, M., Kontomaris, K., Mc Laughlin, J.B., 1998. “Direct numerical simulation of droplet collisions in a turbulent channel flow. Part I: collision algorithm.” Int. Journal of Multiphase Flow **24**, pp.1079-1103.